

Electric bias control on impurity effects in bigraphene

Y.G. Pogorelov,¹ M.C. Santos,² V.M. Loktev^{3,4}

¹*IFIMUP-IN, Departamento de Física, Universidade do Porto,
Rua do Campo Alegre 687, Porto 4169-007, Portugal,*

²*Departamento de Física, Universidade de Coimbra, R. Larga, Coimbra 3004-535, Portugal,*

³*Bogolyubov Institute for Theoretical Physics, NAN of Ukraine, 14b Metrologichna str., Kiev 03680, Ukraine*

⁴*National Technical University of Ukraine KPI, Pr. Peremogy 37, Kiev 03056, Ukraine*

Formation of localized impurity levels within the band gap in bigraphene under applied electric field is considered and the conditions for their collectivization at finite impurity concentration are established. It is shown that a qualitative restructuring of quasiparticle spectrum within the initial band gap and then specific metal-insulator phase transitions are possible for such disordered system at given impurity perturbation potential and concentration, such processes being effectively controlled by variation of the electric field bias. Since these effects can be expected at low enough impurity concentrations and accessible applied voltages, being stable enough thermally, they can be promising for practical applications in nanoelectronics devices.

PACS numbers: 74.70.Xa, 74.62.-c, 74.62.Dh, 74.62.En

1. INTRODUCTION

Between various derivatives from the basic graphene system¹⁻³, a special interest is attributed to its bilayer combination, the bigraphene⁴. This interest is mainly due to the important possibility to realize here a case of semiconductor with controllable band gap through the application of an electric field⁵⁻⁷. It should be noted that similar crystalline structure of two planes with hexagonal lattices is now recognized for a whole family of materials, either really fabricated or theoretically predicted. Besides the two known modifications of bigraphene itself, the Bernal (or A-B) structure⁸ and its alternative, A-A structure⁹, there exist also the bilayers of silicene, the silicon analog to graphene¹⁰, the bilayers of boron nitride¹¹ or its bilayered combination with graphene¹², the bilayered chalcogenides of transition metals (pure or alloyed)¹³, etc. However, the most reliable structure for external tuning and the simplest for theoretical study is seen in the Bernal-stacked bigraphene, hence chosen here as the basic host system for studying impurity effects. By an analogy with the known effects of dopants in common semiconductor systems, this opens a possibility for specific localized impurity levels to exist within the host spectrum gap^{14,15}, like those known for common donor and acceptor levels by impurities in conventional semiconductors with fixed band structure^{16,17}. Next, it is known that, at high enough impurity concentration, an intensive interaction between the localized impurity states related to these levels can take place, and this can essentially modify the band spectrum near the gap edge^{18,21}, giving rise to specific narrow energy ranges of band-like states near impurity levels (called impurity bands) and even producing a phase transition from insulating to metallic state²² with important practical applications. Then the case of in-gap impurity states in

bigraphene could provide an even more flexible field of electronic properties due to the possibility of continuous control on band gap, thus permitting controllable phase transitions. Such situation was recognized long ago in some magnetic crystals with impurities where the magnetic excitation spectra and so the observable properties are controllable by applied magnetic field²³. To the authors' knowledge, such a possibility has not been known before for fermionic systems, and it could open interesting perspectives for future nanoelectronics.

The paper is organized as follows. In Sec. 2, the second quantization Hamiltonian is defined for a Bernal-stacked biased bigraphene (free from impurities) and the related matrix representation for Green functions (GF) is built, giving rise to its 4-subband electronic spectrum. Sec. 3 introduces the model impurity perturbation and studies formation of impurity levels and the conditions for their possible development into impurity bands, based on specific forms of self-energy matrices present in the GF matrices. A more detailed study on such impurity bands, including the estimates for characteristic mobility edges between their ranges of band-like and localized states, is done in Sec. 4. Then the possibility for specific metal-insulator phase transitions in doped bigraphene under variation of external electric field bias (at fixed impurity concentration) and the resulting transport effects are considered in Sec. 5. The final Sec. 6 discusses the main conclusions and suggestions for practical applications of the described impurity effects.

2. BIGRAPHENE UNDER APPLIED FIELD

As is well known, the relevant electronic dynamics of a graphene sheet are generated by the carbon sp^3 orbitals (whose energy level can be chosen as the energy reference) in the simplest approximation of single hopping parameter t between nearest neighbor carbons from different sublattices at distance a in the honeycomb

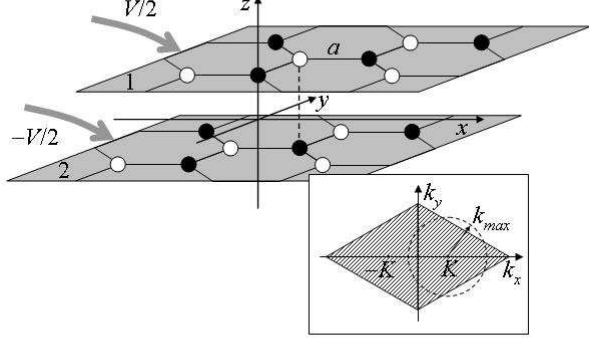


FIG. 1: Schematic of Bernal-stacked bigraphene under applied electric bias V . The A- and B-type sites in each plane are indicated by black and white circles respectively, the solid and dashed lines indicate the in-plane t and interplane t_z links. Inset: the Brillouin zone in \mathbf{k} -plane with two Dirac points $\pm\mathbf{K}$ and an equivalent circle of radius $k_{max} = \sqrt{K/a}$.

lattice². The bigraphene structure, furthermore, involves the interlayer hopping t_z by vertical links between nearest neighbors from different sublattices (for Bernal stacking) shown in Fig. 1. With an account taken of an electric bias $V = eEd$ between the layers (with the electron charge e , the applied electric field E , and the interlayer spacing d), this defines the tight-binding (Fourier transformed) Hamiltonian 4×4 matrix:

$$\hat{H}_{\mathbf{k}} = \begin{pmatrix} V/2 & \gamma_{\mathbf{k}} & 0 & t_z \\ \gamma_{\mathbf{k}}^* & V/2 & 0 & 0 \\ 0 & 0 & -V/2 & \gamma_{\mathbf{k}} \\ t_z & 0 & \gamma_{\mathbf{k}}^* & -V/2 \end{pmatrix}. \quad (1)$$

Here the wave vector \mathbf{k} lies in the first Brillouin zone (see inset in Fig. 1) and the in-plane dispersion follows from the sums $\gamma_{\mathbf{k}} = t \sum_{\delta} e^{i\mathbf{k} \cdot \delta}$ over nearest neighbor vectors δ of the honeycomb lattice, suitably approximated as $\gamma_{\mathbf{k}} \approx \xi_{\mathbf{k}} e^{i\varphi_{\mathbf{k}}}$ with $\xi_{\mathbf{k}} = \hbar v_F |\mathbf{k} - \mathbf{K}|$, the Fermi velocity $v_F = 3ta/2\hbar$, and $\varphi_{\mathbf{k}} = \arctan k_y/(k_x - K_x)$ near the Dirac points $\mathbf{K} = \pm(4\pi/3\sqrt{3}a, 0)$ (the relevant range of $|\mathbf{k} - \mathbf{K}| \sim Kt_z/W$ is really narrow, since t_z is weak besides the total bandwidth W , see below). This matrix enters the second-quantization Hamiltonian (in absence of impurity perturbation):

$$H_0 = \sum_{\mathbf{k}} \psi_{\mathbf{k}}^{\dagger} \hat{H}_{\mathbf{k}} \psi_{\mathbf{k}}, \quad (2)$$

where the spinors $\psi_{\mathbf{k}}^{\dagger} = (a_{1\mathbf{k}}^{\dagger}, b_{1\mathbf{k}}^{\dagger}, a_{2\mathbf{k}}^{\dagger}, b_{2\mathbf{k}}^{\dagger})$ are made of Fourier transformed second quantization operators $a_{j\mathbf{k}} = N^{-1} \sum_{\mathbf{n}} a_{j\mathbf{n}} e^{i\mathbf{k} \cdot \mathbf{n}}$ and $b_{j\mathbf{k}} = N^{-1} \sum_{\mathbf{n}} b_{j\mathbf{n}} e^{i\mathbf{k} \cdot \mathbf{n}}$ with the on-site operators $a_{j\mathbf{n}}$ and $b_{j\mathbf{n}}$ for A- and B-type sites respectively from n th unit cell in $j(=1,2)$ -th layer and

N is the number of cells in a layer. Generally, the energy spectrum is defined through the matrix of Fourier transformed two-time GFs^{24,25} $\hat{G}_{\mathbf{k}} = \langle\langle \psi_{\mathbf{k}} | \psi_{\mathbf{k}}^{\dagger} \rangle\rangle$, as solutions of the dispersion equation:

$$\text{Re det } \hat{G}_{\mathbf{k}}^{-1} = 0. \quad (3)$$

Thus, for the non-perturbed system by Eq. 2 the GF matrix reads $\hat{G}_{\mathbf{k}}^{(0)} = (\varepsilon - \hat{H}_{\mathbf{k}})^{-1}$ and, after diagonalization of $\hat{H}_{\mathbf{k}}$ in spinor indices, its dispersion near the Dirac points is suitably expressed through the radial variable $\xi_{\mathbf{k}} \equiv \xi$. It includes two positive energy subbands:

$$\varepsilon_{\nu}(\xi) = \sqrt{\frac{t_z^2}{2} + \frac{V^2}{4} + \xi^2 - (-1)^{\nu} \sqrt{\frac{t_z^4}{4} + \xi^2 (t_z^2 + V^2)}}, \quad (4)$$

the "external" ($\nu = 1$) and "internal" ($\nu = 2$) ones, and their negative energy counterparts, as shown in Fig. 2a. The most relevant feature of this spectrum is the bias-controlled energy gap between the extrema $\pm\varepsilon_g = \pm V/(2\sqrt{1 + (V/t_z)^2})$ of two internal subbands, attained along a circle around each Dirac point (the so-called "mexican hat") whose radius in the ξ -variable is $\xi_0 = \sqrt{\varepsilon_g^2 + V^2/4}$.

The physical characteristics of this system follow from the GF matrix as, for instance, the density of states (DOS) by electronic quasiparticles:

$$\rho(\varepsilon) = \frac{1}{\pi} \text{Im Tr } \hat{G}(\varepsilon), \quad (5)$$

where $\hat{G}(\varepsilon) = (2N)^{-1} \sum_{\mathbf{k}} \hat{G}_{\mathbf{k}}(\varepsilon)$ is the local GF matrix, and its imaginary part for exact band spectrum results as usually from infinitesimal imaginary shift of energy argument, $\varepsilon - i0^{25}$. In what follows, the sum in \mathbf{k} over triangular halves of the Brillouin zone is approximated by the ξ -integration:

$$\frac{1}{2N} \sum_{\mathbf{k}} f_{\mathbf{k}}(\varepsilon) \approx \frac{2}{W^2} \int_0^W f(\xi, \varepsilon) \xi d\xi,$$

over two equivalent circles around Dirac points (inset in Fig. 1) of the ξ -radius $W = \hbar v_F k_{max}$ (where $k_{max} = \sqrt{K/a}$, see inset in Fig. 1), well justified at low energies, $|\varepsilon| \ll W$. For the pure bigraphene system by Eq. 1, the result for Eq. 5 is generated by the explicit diagonal elements of non-perturbed local GF matrix¹⁴:

$$\begin{aligned} G_{11}^{(0)} &\approx 2 \frac{\varepsilon - \varepsilon_2}{W^2} \left[\frac{\varepsilon \varepsilon_2}{\delta^2} \left(\pi - \arctan \frac{\delta^2}{\varepsilon^2 + \varepsilon_2^2} \right) + \ln \frac{\gamma}{W} \right], \\ G_{22}^{(0)} &= G_{11}^{(0)}(\varepsilon) - t_z^2 \frac{\varepsilon + \varepsilon_2}{W^2 \delta^2} \left(\pi - \arctan \frac{\delta^2}{\varepsilon^2 + \varepsilon_2^2} \right), \end{aligned} \quad (6)$$

where

$$\begin{aligned} \delta^2(\varepsilon) &= \sqrt{(t_z^2 + V^2)(\varepsilon_g^2 - \varepsilon^2)}, \\ \gamma^2(\varepsilon) &= \sqrt{(\varepsilon^2 - \varepsilon_1^2)(\varepsilon^2 - \varepsilon_2^2)}. \end{aligned}$$

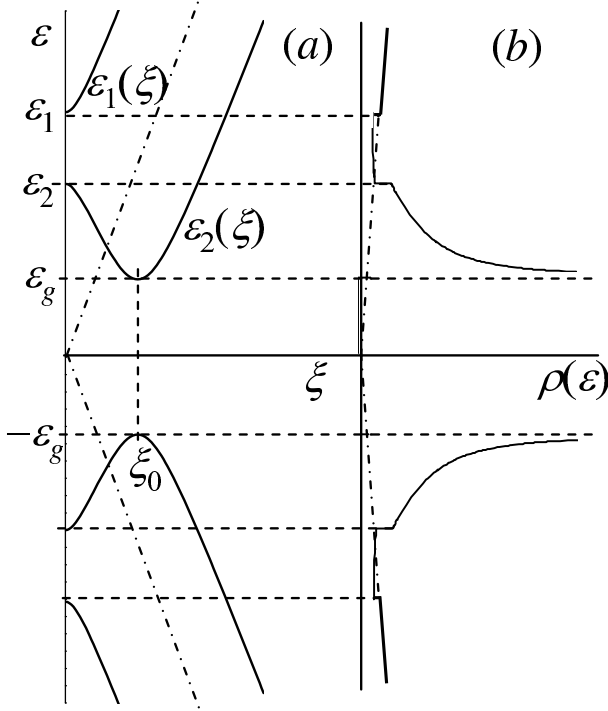


FIG. 2: a) Dispersion laws for the bilayer in Fig. 1 vs the radial variable ξ near a Dirac point, given by Eq. 4 at the choice of $V = 2t_z$, the dash-dotted line indicate the Dirac dispersion for monolayered graphene. b) DOS for this choice, the dash-dotted line marks the linear DOS for monolayered graphene.

These elements reveal the inverse square root divergences at the gap edges $\pm\epsilon_g$ (of $\text{Im } G$ beyond the gap and of $\text{Re } G$ within the gap), also note the finite steps of $\text{Im } G$ at the limiting energies $\epsilon_{1,2} \equiv \epsilon_{1,2}(0)$ of the two subbands. The resting diagonal elements are simply $G_{33}^{(0)}(\epsilon) = -G_{22}^{(0)}(-\epsilon)$ and $G_{44}^{(0)}(\epsilon) = -G_{11}^{(0)}(-\epsilon)$, so that finally DOS is a function of ϵ^2 , as shown in Fig 2b in agreement with the known previous calculations⁷. It presents BCS-like divergences near ϵ_g^2 , finite steps at $\epsilon_{1,2}^2$, and gets to coincidence with the linear DOS for monolayer graphene^{2,3} beyond ϵ_1^2 , due to joint (non-linear) contributions from both subbands.

Within the gap, only real parts of $G_{jj}(\epsilon)$ are non-zero, and their divergences near the gap edges are crucial for appearance, under the effect of localized impurity perturbations, of in-gap localized levels and related collective states which is the main focus for the analysis below.

3. IMPURITY LEVELS AND IMPURITY SUBBANDS

As was recognized from experimental studies on graphene systems²⁶, they can contain a variety of defects, ranging from topological ones (vacancies, dislocations, edges, boundaries, etc.) to impurity adatoms

(or some functional groups) near one of planes and in-plane substitutes or interstitials. This provides a doping of charge carriers (of both signs) into these systems as well as scattering of carriers on impurity potentials and possibly formation of localized (or resonance) impurity states on such potentials. The latter must be characterized by some model parameters within the common tight-binding approximation and the simplest case is the Lifshitz model only involving the on-site perturbation potential U , identical for all impurity sites randomly distributed among the lattice sites²⁷. This model with moderate U value (comparable with the graphene bandwidth W) looks more adequate to the case of substitutional impurities in graphene, than its unitary limit, $U \gg W$ in Ref.²⁸ or the alternative choice of Anderson model²⁹ with random perturbations at each lattice site in Ref.³⁰. Another alternative is the Anderson hybrid (or s - d) model³¹ with two parameters, the impurity binding energy and its coupling to the host excitations, and its use for the so called deep impurity levels in semiconductors is known to result in formation of the above mentioned impurity bands and related phase transitions. However, such perturbation model when introduced into the framework of 4-component host spectrum of Sec. 2 could make the most important treatment of interactions between impurities and of impurity band coherence technically unfeasible. This determines our choice for the Lifshitz model (though known to provide less freedom for impurity bands formation than the s - d model). By similar reasons, we do not consider the long-range impurity potentials as for Coulomb^{32,33} or screened-Coulomb³⁴ centers.

Let us build the perturbation Hamiltonian by Lifshitz impurities on certain impurity sites. In accordance with the composition of ψ -spinors, the A- and B-sites from first plane can be referred to the types $j = 1, 2$ respectively and those from second plane to $j = 3, 4$, then \mathbf{p}_j denote the defect sites of j th type with relative concentrations $c_j = \sum_{\mathbf{p}_j} N^{-1}$ such that the total impurity concentration $\sum_j c_j = c \ll 1$. Then the sought Hamiltonian in terms of local Fermi operators reads

$$H_1 = U \left(\sum_{\mathbf{p}_1} a_{1\mathbf{p}_1}^\dagger a_{1\mathbf{p}_1} + \sum_{\mathbf{p}_2} b_{1\mathbf{p}_2}^\dagger b_{1\mathbf{p}_2} + \sum_{\mathbf{p}_3} a_{2\mathbf{p}_3}^\dagger a_{2\mathbf{p}_3} + \sum_{\mathbf{p}_4} b_{2\mathbf{p}_4}^\dagger b_{2\mathbf{p}_4} \right), \quad (7)$$

or, in terms of ψ -spinors by Eq. 2, it takes the form of scattering operator:

$$H_1 = \frac{1}{N} \sum_{j, \mathbf{p}_j} \sum_{\mathbf{k}, \mathbf{k}'} e^{i(\mathbf{k}' - \mathbf{k}) \cdot \mathbf{p}_j} \psi_{\mathbf{k}}^\dagger \hat{U}_j \psi_{\mathbf{k}'}. \quad (8)$$

where the diagonal matrix \hat{U}_j has a single non-zero element U at the jj site. Considering now the Hamiltonian in presence of impurities $H_0 + H_1$ and following a similar routine to Refs.^{35,36}, we arrive at solutions for the GF

matrix in two specific forms adequate for two alternative types of excitation states in a disordered system^{22,27}, the band-like (extended) states and localized states. Thus, the first of these types is better described by the so-called fully renormalized representation (FRR) of GF²³:

$$\hat{G}_{\mathbf{k}} = \left[\left((\hat{G}_{\mathbf{k}}^{(0)})^{-1} - \hat{\Sigma}_{\mathbf{k}} \right)^{-1} \right] \quad (9)$$

where the self-energy matrix is additive in different types of impurity centers: $\hat{\Sigma}_{\mathbf{k}} = \sum_j \hat{\Sigma}_{j,\mathbf{k}}$, with the partial matrices given by the related FRR group expansions (GE's) in complexes of impurity centers (of the same j -type, involved in multiple scattering processes):

$$\begin{aligned} \hat{\Sigma}_{j,\mathbf{k}} = & c_j \hat{T}_j \left[1 + c_j \sum_{\mathbf{n} \neq 0} \left(e^{-i\mathbf{k} \cdot \mathbf{n}} \hat{A}_{j,\mathbf{n}} + \hat{A}_{j,\mathbf{n}} \hat{A}_{j,-\mathbf{n}} \right) \right. \\ & \times \left. \left(1 - \hat{A}_{j,\mathbf{n}} \hat{A}_{j,-\mathbf{n}} \right)^{-1} + \dots \right]. \end{aligned} \quad (10)$$

Each T-matrix $\hat{T}_j = \hat{U}_j \left(1 - \hat{G} \hat{U}_j \right)^{-1}$ describes all the scatterings on a single impurity center of j th type, and the next to unity term in r.h.s. of Eq. 10 accounts for scatterings on pairs of j -impurities through the matrices $\hat{A}_{j,\mathbf{n}} = \hat{T}_j (2N)^{-1} \sum_{\mathbf{k}' \neq \mathbf{k}} \hat{G}_{\mathbf{k}'} e^{i\mathbf{k}' \cdot \mathbf{n}}$ of indirect interaction (via band-like excitations) in such pairs at separation \mathbf{n} . Notice the excluded quasimomentum \mathbf{k} (for given $\hat{\Sigma}_{\mathbf{k}}$) in this sum, also the FRR GE excludes coinciding quasimomenta in all the multiple sums for products of interaction matrices²³. The omitted terms in Eq. 10 relate to all scattering processes in groups of three and more impurities, and their general structure can be found in similarity with the known group integrals from the Ursell-Mayer classical theory of non-ideal gases.

Otherwise, for the range of localized states, the non-renormalized representation (NRR):

$$\hat{G}_{\mathbf{k}} = \hat{G}_{\mathbf{k}}^{(0)} - \hat{G}_{\mathbf{k}}^{(0)} \hat{\Sigma} \hat{G}_{\mathbf{k}}^{(0)}, \quad (11)$$

is more adequate. Here the respective NRR self-energy matrix $\hat{\Sigma} = \sum_j \hat{\Sigma}_j$ has a similar structure to the FRR one by Eq. 10 but with the NRR matrices $\hat{T}_j^{(0)} = \hat{U}_j (1 - \hat{G}^{(0)} \hat{U}_j)^{-1}$, $\hat{G}^{(0)} = (2N)^{-1} \sum_{\mathbf{k}} \hat{G}_{\mathbf{k}}^{(0)}$, and with no restrictions in all the quasimomentum sums for the products of NRR interaction matrices $\hat{A}_{j,\mathbf{n}}^{(0)} = \hat{T}_j^{(0)} (2N)^{-1} \sum_{\mathbf{k}} \hat{G}_{\mathbf{k}}^{(0)} e^{i\mathbf{k} \cdot \mathbf{n}}$ (that are only present in their even combinations $\hat{A}_{j,\mathbf{n}}^{(0)} \hat{A}_{j,-\mathbf{n}}^{(0)}$). The best known effect of local perturbations consists in emergence of localized energy levels within the band gap and those were already indicated for impurities in bigraphene^{14,15}. As known from general theory^{23,27}, such levels are most pronounced at sufficiently low concentration of impurities (so that their indirect interactions can be neglected) and given by the poles of T-matrices. In the present case, the matrices $\hat{T}_j^{(0)}$ give rise to four different local levels $\varepsilon^{(j)}$ within the band

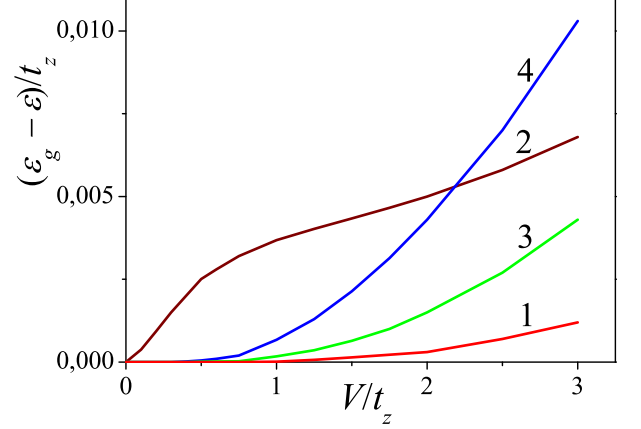


FIG. 3: Separations of the in-gap impurity levels $\varepsilon^{(j)}$ from the gap edge as functions of the applied bias V (all in units of t_z , the curves being labeled by the j numbers). Note the different behavior of $\varepsilon^{(1,2)}$ levels from that of $\varepsilon^{(3,4)}$ ones and the resulting interchange of the deepest levels at the bias value $V_{cr} \approx 2.2t_z$ (see also the text).

gap, and their locations depend on the magnitude and sign of perturbation parameter U (like the known situations in common doped semiconductors^{16,17}) but yet on the applied field V (as a specifics of doped bigraphene). The positions of four impurity levels $\varepsilon^{(j)}$ by each type of impurity center are the roots of related Lifshitz equations:

$$UG_{jj}^{(0)}(\varepsilon^{(j)}) = 1, \quad (12)$$

so that choosing for definiteness $U = -W/2$ and using Eq. 6 provides their dependence on the applied bias V as shown in Fig. 3 (for their relative separations from the gap edge). It is seen that generally they stay rather shallow at growing V , but with a notable difference between the levels $\varepsilon^{(1,2)}$ (by impurities in the positive biased layer) and $\varepsilon^{(3,4)}$ (by those in the negative biased one). In particular, a specific interchange of the deepest levels occurs in this course, from $\varepsilon^{(2)}$ to $\varepsilon^{(4)}$, at $V_{cr} \approx 2.2t_z$ for given U . This feature was not indicated in the former analysis of the same model in Ref.¹⁴, where $\varepsilon^{(4)}$ was considered to remain the deepest level at all V values. Also, it can be noted that for the commonly used value of $t_z \approx 0.35$ eV this interchange bias would amount to $V_{cr} \approx 0.77$ eV, well above the experimentally realized (to the moment) V values of up to ≈ 0.36 eV⁵. Thus, the much stronger separation of the $\varepsilon^{(2)}$ level at lower bias voltages could be of significant practical importance.

The well known property of localized states by shallow energy levels is their long effective radius²³, also indicated for impurities in biased bigraphene¹⁴, defining intensive interactions between them already at their very low concentrations. Such interactions were shown to allow, at certain conditions, collectivization of impu-

rity states to form specific band-like states within narrow energy bands (called impurity bands) around the initial localized levels¹⁸. As will be seen below, this effect is possible as well in the present case of multiple localized levels, where the most essential specifics is their joint participation in forming the lowest impurity subband of much stronger dispersion than in higher lying subbands (if those are permitted).

Formally, in similarity to the non-perturbed case, the band spectrum for the disordered system can be evaluated from the dispersion equation, Eq. 3, with the GF matrix by FRR Eqs. 9,10. Of course, if treated rigorously, it presents a tremendous problem of developing infinite sequence of renormalization procedures in all possible terms of the corresponding GE, and there is no reasonable hope for its exact solution. The popular way to avoid this problem is restriction of the full self-energy to its self-consistent T-matrix form (that is, neglecting all the interactions between impurities) known as the coherent potential approximation (CPA)¹⁹ and it was suggested for studies of disorder effects both in monolayer graphene²⁰ and bigraphene¹⁴. Although this approach describes certain impurity bands, it is known to fail just in reproducing the observed (when available) narrow dispersion of these bands. On the other hand, validity of the simplest NRF, Eq. 11, is only limited to the energy ranges of fully localized states.

A more consistent approach can be suggested using partial renormalizations of the full self-energy in Eq. 10, first substituting there the NRR T-matrix and interaction matrices and then subsequently introducing such approximate self-energies into the next generations of GF and interaction matrices, checking convergence of the obtained GE's in order not to extend the renormalizations to irrelevant GE terms. Namely, it is reasonable to define the l th generation GF matrix $\hat{G}_{\mathbf{k}}^{(l)}$ by an analog to Eq. 9 with the respective self-energy $\hat{\Sigma}_{\mathbf{k}}^{(l)}$ by an analog to Eq. 10 but containing T-matrices $\hat{T}^{(l-1)}$ and interaction matrices $\hat{A}_{\mathbf{n}}^{(l-1)}$ built with use of the preceding generation $\hat{G}_{\mathbf{k}}^{(l-1)}$ matrices. This algorithm leads to the true FRR at $l \rightarrow \infty$. However, even its first non-trivial $l = 1$ approximation can be reasonable for the band-like energy ranges where the true FRR GE converges.

Then, in the first step of this routine, the formal solutions of Eq. 10 with the self-energies in the NRR T-matrix approximation, $\hat{\Sigma}_{j,\mathbf{k}} \approx c_j \hat{T}_j^{(0)}$, display four narrow subbands near four impurity levels $\varepsilon^{(j)}$, besides the four broad principal bands $\pm \varepsilon_{\nu}(\xi)$ (here only slightly modified compared to Eq. 4). An example of such modified spectrum (at a natural choice of equal partial concentrations $c_j = c$ and taking the total impurity concentration $4c = 0.01$) for the cases of Fig. 3 is shown in Fig. 4. The lowest impurity subband, conventionally denoted here as $\varepsilon^{(2)}(\xi)$ by its proximity to the lowest $\varepsilon^{(2)}$ level, is seen to strongly dominate in its dispersion over all the resting ones, and the direct analysis of Eq. 10 shows that this domination is due to the above mentioned construc-

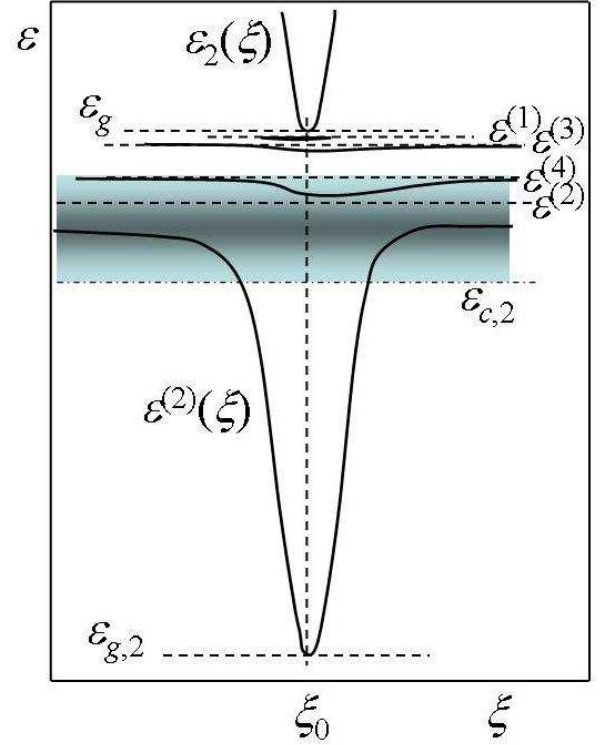


FIG. 4: Formation of impurity subbands near the impurity levels by the solutions of Eq. 3 in the 1st step of renormalization (see text) for the case of Fig. 3 at $V = 2t_z$. The most dispersive $\varepsilon^{(2)}(\xi)$ subband extends well beyond the shadowed vicinity of the $\varepsilon^{(2)}$ level, that delimits the range of localized states down to the respective mobility edge $\varepsilon_{c,2}$. Similar localized areas around $\varepsilon^{(4,3,1)}$ (not shown here) would continuously extend this range up to above the gap edge ε_g .

tive interplay between all $\varepsilon^{(j)}$.

Note that all the impurity subbands in this approximation produce BCS-like divergences in DOS, as well near the levels $\varepsilon^{(j)}$ as near subbands terminations. However, since quasimomentum is not true quantum number in a disordered system²⁷, the analysis of its real energy spectrum, especially for the in-gap states, should also take account of the damping $\Gamma_j(\xi)$ of each $\varepsilon^{(j)}(\xi)$ state, resulting from $\text{Im} \Sigma_j$. Hence one can consider these states Bloch-like (or conducting) only if the Ioffe-Regel-Mott (IRM) criterion^{22,37} is fulfilled or the GE, Eq. 10, is convergent at related energies. Otherwise they should pertain to the localized type. As will be seen, all the formal DOS singularities fall within the localized energy ranges and so are effectively broadened.

The mentioned criteria permit to estimate also the division points between band-like and localized ranges known as Mott's mobility edges²². Of course, such mobility edges can be found near the limits of both principal and impurity bands, but our main focus here will be on the most dispersive impurity band, like $\varepsilon^{(2)}(\xi)$ in the above example, as the most interesting object for practical purposes. Finally, a certain special value V_A of bias

control (at given impurity concentrations c_j and perturbation parameter U) can be indicated, such that mobility edges from both sides of a conducting impurity band will merge. This collapse of impurity band will manifest a kind of Anderson transition²⁹ in a disordered system, realized in a controllable way at $V \rightarrow V_A$.

It should be underlined that all these fundamental features of the energy spectrum in a disordered system are fully ignored when the narrow impurity bands are treated using the CPA approximation (as, e.g., in Refs.^{14,20}) beyond its known validity checks³⁸.

4. CONDITIONS FOR EXISTENCE OF IMPURITY SUBBANDS

As known from studies on many disordered systems where a localized impurity level ε_{imp} near an edge ε_g of pure crystal energy band can give rise, at high enough impurity concentration, to a specific impurity band $\varepsilon_{imp}(\mathbf{k})$ ²³, the latter is restricted by the general IRM criterion:

$$\mathbf{k} \cdot \nabla_{\mathbf{k}} \varepsilon_{imp}(\mathbf{k}) \gg \Gamma_{imp}(\varepsilon_{imp}(\mathbf{k})), \quad (13)$$

where the linewidth $\Gamma_{imp}(\varepsilon)$ of a Bloch-like state with quasi-momentum \mathbf{k} and energy ε is defined as the imaginary part of the corresponding self-energy. For the present multiband system, this criterion should be formulated for each of $\varepsilon^{(j)}(\varepsilon)$ subbands by expanding the general determinant from Eq. 3 near a given energy ε in a complex form: $\det \hat{G}_{\mathbf{k}}^{-1} \approx [\varepsilon - \varepsilon^{(j)}(\varepsilon) + i\Gamma_j(\varepsilon)] \Omega_j(\varepsilon)$, to obtain the corresponding linewidth $\Gamma_j(\varepsilon)$ (aside a certain factor $\Omega_j(\varepsilon)$ of energy to cube dimension).

In the adopted Lifshitz model, each partial T-matrix \hat{T}_j (regardless of its renormalization) has a single non-zero element at the jj site (alike \hat{U}_j itself): $T_j = U/(1 - UG_{jj})$. In the above suggested first step renormalization, we have $\text{Im}T_j^{(0)} = 0$ for ε within the bandgap. Then the imaginary part of related self-energy function $\Sigma_j^{(1)}$ is here only due to the GE terms next to unity in Eq. 10, dominated by the pair term once GE is convergent. It can be also shown that the most relevant contribution to $\text{Im}\Sigma_j(\varepsilon)$ comes from the jj th matrix element of the GE pair term while those from its other elements (though generally non-zero) are strongly reduced by the quantum interference effects. This contribution:

$$B_j(\varepsilon) = \text{Im} \sum_{n>a} \frac{A_{j,\mathbf{n}}^{(0)} A_{j,-\mathbf{n}}^{(0)}}{1 - A_{j,\mathbf{n}}^{(0)} A_{j,-\mathbf{n}}^{(0)}}, \quad (14)$$

can be obtained from the residues at zeroes of the denominator, using the explicit spatial behavior of scalar

interaction functions (see Appendix A for details):

$$\begin{aligned} A_{j,\mathbf{n}}^{(0)}(\varepsilon) &= \frac{T_j^{(0)}(\varepsilon)}{2N} \sum_{\mathbf{k}} e^{i\mathbf{k} \cdot \mathbf{n}} \left(G_{\mathbf{k}}^{(0)} \right)_{jj} \\ &\approx \sqrt{\frac{r_{j,\varepsilon}}{n}} e^{-n/r_\varepsilon} \sin \frac{n}{r_0} \cos \mathbf{K} \cdot \mathbf{n}, \end{aligned} \quad (15)$$

where the characteristic scales are:

$$r_{j,\varepsilon} = r_0 \left(\pi \frac{\varepsilon_g - \varepsilon^{(j)}}{\varepsilon - \varepsilon^{(j)}} \right)^2, \quad r_\varepsilon = r_0 \frac{\xi_0^2}{\delta^2}, \quad r_0 = \frac{\hbar v_F}{\xi_0}.$$

A similar behavior with two oscillating factors in effective inter-impurity interactions was previously indicated for the impurity states within superconducting gap in ferropnictides³⁵ where a faster cosine factor had Fermi wavelength. But, the present case is simplified by the specific symmetry of \mathbf{K} in the Brillouin zone, so that $\cos^2 \mathbf{K} \cdot \mathbf{n}$ for all separations \mathbf{n} between lattice sites of the same j th type only takes the values $\sigma = 1$ and $1/4$ (with respective weights $p_\sigma = 1/3$ and $2/3$) whose contributions can be then simply added up in Eq. 14. These partial contributions are obtained by subsequent integrations³⁵, first over the poles of fast oscillating sine and then over its residues with the slow envelope function $F_{j,n,\sigma}^2 = \sigma r_{j,\varepsilon} e^{-2n/r_\varepsilon} / n$:

$$\begin{aligned} B_j &= \sum_{\sigma} p_{\sigma} \text{Im} \sum_{n>a} \frac{F_{j,n,\sigma}^2 \sin^2(n/r_0)}{1 - F_{j,n,\sigma}^2 \sin^2(n/r_0)} \\ &\approx \sum_{\sigma} \frac{4\pi p_{\sigma}}{\sqrt{3}a^2} \int_a^{r_{max}} \frac{r dr}{\sqrt{F_{j,r,\sigma}^2 - 1}}, \end{aligned} \quad (16)$$

where r_{max} corresponds to $F_{j,r_{max}} = 1$. The latter integration is simplified within the energy range of:

$$\varepsilon^{(j)} - \varepsilon \gg (\varepsilon_g - \varepsilon^{(j)})^{5/4} / \varepsilon_g^{1/4}, \quad (17)$$

where $r_{j,\varepsilon} \ll r_\varepsilon$ so that the exponential factor in Eq. 15 remains approximately unity for all distances $r < r_{max} \approx r_{j,\varepsilon}$. In this approximation, the explicit result for the most dispersive subband reads:

$$B_2(\varepsilon) = \frac{7\pi}{64} \left(\frac{r_{2,\varepsilon}}{a} \right)^2, \quad (18)$$

with the prefactor resulted precisely from weighting of σ values. Then the above suggested expansion of $\det \hat{G}_{\mathbf{k}}^{-1}$ for ε closer to $\varepsilon^{(2)}$ than to other $\varepsilon^{(j)}$ (so that all Σ_j except Σ_2 can be neglected) provides the linewidth:

$$\Gamma_2(\varepsilon) \approx c^2(\varepsilon^{(2)} - \varepsilon) B_2(\varepsilon), \quad (19)$$

valid until $\varepsilon^{(2)} - \varepsilon \lesssim \varepsilon_g - \varepsilon^{(2)}$. For ε yet farther from $\varepsilon^{(2)}$, we have $r_{j,\varepsilon} < r_0$ so that $B_2(\varepsilon)$ vanishes and finite Γ_2 values can only result from the higher order GE terms (if we exclude, of course, all other possible relaxation processes, such as thermal phonons, electron-electron collisions, etc.). From Eq. 19, the IRM criterion is reduced to the inequality:

$$c B_2(\varepsilon) \ll 1$$

(agreeing with the GE convergence) and, supposing Eq. 17 valid, this criterion permits to estimate the mobility edge separation from the $\varepsilon^{(2)}$ level:

$$\varepsilon^{(2)} - \varepsilon_{c,2} \sim c^{1/4} \sqrt{\frac{W}{2\xi_0}} (\varepsilon_g - \varepsilon^{(2)}). \quad (20)$$

All the states with energies closer to $\varepsilon^{(2)}$ than $\varepsilon_{c,2}$ are localized on various clusters of 2nd type impurity centers. The first conclusion from the estimate, Eq. 20, is that existence of the impurity subband itself is only assured if its bandwidth $\approx \varepsilon^{(2)} - \varepsilon_{g,2}$ surpasses the width of localized range around $\varepsilon^{(2)}$. This is fulfilled when the total impurity concentration exceeds the critical value:

$$c_{cr} \sim \left(\frac{t_z}{W}\right)^{8/3} \left(\frac{|U|}{W}\right)^{4/3} \left(\frac{V}{W}\right)^{2/3} \times \frac{(t_z + \sqrt{t_z^2 + V^2})(2t_z^2 + V^2)}{(t_z^2 + V^2)^{2/3} t_z^{5/3}}, \quad (21)$$

(it is obtained approximating Eq. 6 only to its diverging terms). Smallness of this expression is mainly due to its first three essential factors of interlayer coupling, impurity perturbation, and applied bias, while the last factor stays almost constant for all realistic (not too high) V . Thus, for the sample choice of parameters, $W = 20t_z$, $|U| = 10t_z$, and $V = 2t_z$, we obtain $c_{cr} \sim 1.8 \cdot 10^{-5}$. Then for the example of $c = 0.01$ chosen in Fig. 3, the mobility edge $\varepsilon_{c,2}$ extends from $\varepsilon^{(2)}$ to about 0.38 of the distance $\varepsilon_g - \varepsilon^{(2)}$ while the dispersion of $\varepsilon^{(2)}(\xi)$ subband is about four times bigger (see Fig. 4). Finally, from comparison of Eqs. 20 and 17 it follows that for $c > c_{cr}$ the latter vicinity always occurs within the localized range and so the exponential factor in Eq. 15 cannot influence the above obtained estimates. In summary, only the most dispersive impurity subband by the lowest impurity level can be considered to really emerge beyond its mobility edge, with its main specifics in anomalously strong variation of the lifetimes $\tau(\varepsilon)$ along very narrow energy intervals. As to other formal solutions of Eq. 3 (analyzed with inclusion of the resting B_j), they are mostly invalidated within the common overlapped range of higher laying localized levels, that extends up to $\varepsilon_{c,+}$, the mobility edge of the upper main band. The states in this area can be only characterized by their DOS. Though the latter function can not be directly found here from the above defined GE's, Eqs. 9, 11, it can be plausibly expected to vary slowly until matching to the peak near ε_g (Fig. 5), so that the total number of states $\int_{-W}^W \rho(\varepsilon) d\varepsilon = 4$ is kept.

Similarly, some finer details of the energy spectrum can be also determined, such as, for instance, the rest of mobility edges: $\varepsilon_{c,\pm}$, that define the broadened edges of main subbands, and that near the extremum $\varepsilon_{g,2} \approx \varepsilon^{(2)}(\xi_0)$ of the impurity subband (see Fig. 5). At last, the case of low impurity concentration, $c < c_{cr}$, can be also included when there is no impurity band within the

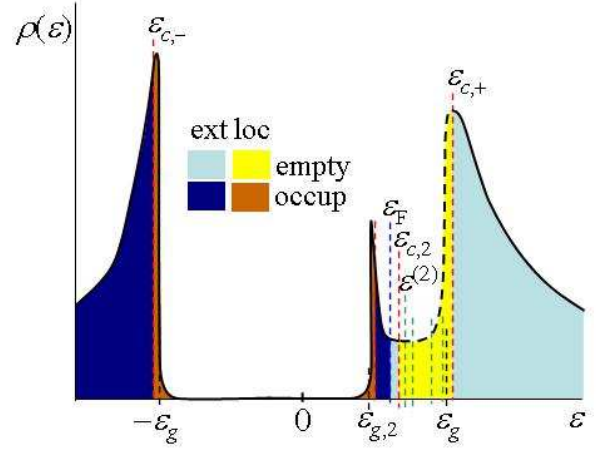


FIG. 5: Schematics of extended (ext) and localized (loc) ranges in the energy spectrum of bigraphene with impurities for the situation alike that in Fig. 4. Note the position of the Fermi level (separating occupied and empty states) with respect to the mobility edges (separating ext and loc states); the narrow impurity band only emerges below the lowest impurity level $\varepsilon^{(2)}$ (the labels for higher $\varepsilon^{(j)}$ are omitted) while the localized states fill the whole range from $\varepsilon_{c,2}$ up to $\varepsilon_{c,+}$ (see in text).

gap but the localized levels $\varepsilon^{(j)}$ turn to be separately resolved. However all these data are not so relevant for our main practical purpose below and so left beyond the present scope. Nevertheless, the presented results give an important extension and diversification of the general scenario of collective restructuring of spectra of elementary excitations in crystals with impurities under external fields²³.

5. BIASED METAL-INSULATOR TRANSITIONS AND THEIR OBSERVABLE EFFECTS

Now we can pass to the important processes of electric transport in the system with the above described band spectrum. For simplicity, this consideration is restricted to the case of zero temperature and the main attention is paid to the position of Fermi level ε_F and to the lifetime τ_F of Fermi states under the applied bias control V at given parameters of impurity perturbations c and U . The basic condition for the Fermi level:

$$2 \int_{-\infty}^{\varepsilon_F} \rho(\varepsilon) d\varepsilon = 1 + c', \quad (22)$$

defines its shift from the zero energy position in the unperturbed system, in order to accommodate the total of c' extra carriers per unit cell (brought by impurities themselves and possibly by some external sources). This generally requires knowledge of DOS functions for all the impurity subbands (besides almost non-perturbed ones

for main subbands). But our main interest here is in finding a possibility for ε_F to be located within the most dispersive impurity band $\varepsilon^{(2)}(\xi)$, so we focus on the related DOS, especially in proximity to this band termination $\varepsilon_{g,2}$ (Fig. 5). An important simplification of this task is obtained by noting that for this energy range all the self-energies Σ_j in Eq. 10 can be taken as constants, small enough compared to the gap width, thus the solutions of the dispersion equation, Eq. 3, almost reproduce here the non-perturbed $\varepsilon_2(\xi)$ band within accuracy to a constant shift of its edge from ε_g to $\varepsilon_{g,2}$ (see Fig. 4), just due to the common effect of all Σ_j . The resulting DOS function:

$$\rho_2(\varepsilon) \approx \frac{2\varepsilon}{W^2} \frac{t_z^2 + V^2}{\delta^2}, \quad (23)$$

at $0 < \varepsilon - \varepsilon_{g,2} \lesssim \varepsilon^{(2)} - \varepsilon_{g,2}$ defines from Eq. 21 the Fermi level ε_F position by the equation

$$c' \approx \left(\frac{2}{W}\right)^2 \sqrt{(t_z^2 + V^2)(\varepsilon_g^2 - \varepsilon_F^2)}. \quad (24)$$

Let c'_{max} be the maximum permitted amount of carriers such that ε_F stays within the conducting range. Then, for the case of Fig. 4, this value results $c'_{max} \approx 4 \cdot 10^{-3}$, that is, somewhat lower than the proper impurity concentration $c = 10^{-2}$ in this case. Nevertheless, conduction through the impurity band can be realized if c' is brought below the indicated limit of c'_{max} , e.g., by external compensation of a part of charge carriers¹⁷. Once this is assured, one can then strongly change the conductivity by raising the applied V , since the localized range width by Eq. 19 grows with bias faster than $\propto V^{2/3}$ against the almost bias insensitive (at $V \lesssim V_{cr}$, see Fig. 3) width of the impurity band, while the Fermi level ε_F goes to the band edge $\varepsilon_{g,2}$ slower than $\propto V^{-2}$. Then the faster advancing mobility edge $\varepsilon_{c,2}$ will finally cross ε_F at some bias V_{M-I} , giving rise to a Mott metal-insulator transition and vanishing conductivity. Thus, for the proposed choice of $U = -W/2 = -10t_z$ and $c' = 3 \cdot 10^{-3}$, we obtain $V_{M-I} \approx 0.87$ eV. In this course, at $V \rightarrow V_{M-I}$, conductivity can vary by orders of magnitude, when we drive the Fermi inverse lifetime $\tau_F^{-1} \sim \Gamma_2(\varepsilon_F)/\hbar$ close to divergence, under very tiny variations (say, some meV) of bias. This indicates a tremendous potentiality of such type of doped semiconducting systems in comparison with traditional materials.

Besides their evident field transistor applications, critical effects by the biased Mott transition can be also expected in other observable properties of this doped system, for instance, in its optical response at the frequency $\omega_{i,b} \approx (\varepsilon^{(2)} + \varepsilon_g)/\hbar$ of transition from the top of occupied $-\varepsilon_2(\xi)$ band and the Fermi states of impurity $\varepsilon^{(2)}(\xi)$ band (like the case formerly considered by the authors for doped superconducting iron pnictides³⁶) that can be switched on and off by tiny variation of the bias.

At last, with further growing bias, the collapse of upper and lower mobility edges within the impurity band and

the aforementioned Anderson transition to fully localized in-gap spectrum can be realized. From Eq. 20 at $V \lesssim t_z$, this bias value estimates as $V_A \sim c^{3/2}W^7|U|^{-2}t_z^{-4}$, though this analytic expression only applies (at moderate $|U|$) for as low impurity concentrations as $c \lesssim 10^{-5}$. However a numerical analysis with use of full Eq. 6 shows that V_A remains attainable up to $c \sim 10^{-2}$ as well. This transition can also produce observable effects; in this case the collapse of narrow impurity band would lead to a dramatic drop of the plasmonic resonance frequency³⁹.

6. DISCUSSION AND CONCLUSIONS

The above main conclusion about the possibility to attain extensive control on electrical conduction through very slight variations of applied potential implies, of course, many additional factors to be taken into account. They can be indicated both from the theoretical and practical sides. Thus, the used theoretical approach is restricted to a simple model of impurity perturbation by a single on-site parameter, and some elaboration of it could be done involving, for instance, perturbations of hopping parameters. These kinds of analyses are known for traditional semiconductors with impurities and also have demonstrated possibility for similar bands of collective states to be formed near localized impurity levels at high enough impurity concentrations. Notably, for those more common materials, it was just the Lifshitz perturbation model that presented the biggest theoretical problems for such effects, for instance, by leading to unrealistically high values of critical concentration, of order of unity or even more (unlike that in Eq. 19). This permits to expect that modifications of the present Lifshitz model, as in Ref.¹⁵ for single impurity at gapless spectrum, or using the Anderson hybrid model³¹ as in Ref.⁴⁰ (provided all the technical aspects be assured) will not change essentially the physical behavior of the system. On the other hand, there are yet many properties of this simple model that can be further studied, for instance, the possibilities to realize multiple conducting impurity subbands and subsequent processes of multiple switching between them, including, e.g., optical transitions under electrical biasing. Of course, a more realistic approach should also take account of topological defects (see beginning of Sec. 3) as well as the above mentioned Coulomb interactions, thermal effects, etc. Generally, this would require the impurity band structure to exceed a certain "background" relaxation level, that could be achieved by varying either the impurity sort (that is, U parameter) and concentration or/and the applied bias V . Finally, similar impurity multiband effects can be also sought in other atomically multilayered systems, such as those mentioned in the Introduction, where a special focus might be put on tuned bandgap in silicene bilayers (yet wider than in bigraphene¹⁰) or even on single layers of buckled silicene or germanene⁴¹.

As to the practical issues, first of all, rather strict con-

ditions on fabrication of the basic doped bilayered system are in order, perhaps mainly aimed to minimize all the "foreign" defects *vs* the chosen dopants, but the next requirement to keep the levels of dopants (and possibly their compensating species) within to fractions of percent should not be a real problem for modern nanoelectronics. A special attention is also required for precise control and manipulation of the applied bias V , particularly, in exploring possibilities to realize its near-critical and super-critical regimes, like those indicated in the above analysis. Finally, the practical arrangement of an experimental transistor-type setup based on the suggested conductivity control by tiny impurity subbands would perhaps require some specific technical solutions. However, they do not look too difficult to be found in the available engineering depository. Thus, a fair hope exists for this theoretical proposal to be realized in a practical device.

In conclusion, the effects of localized on-site perturbations by rather disperse impurities on bilayered graphene system under the applied electrical bias between the layers are theoretically considered using the Green function techniques adapted for a multiband electronic system, demonstrating the conditions for different types of localized impurity energy levels to appear within the bias-induced bandgap in the electronic spectrum of this system and then extension of these levels into specific narrow energy bands at impurity concentration surpassing certain characteristic values. The analysis on these pro-

cesses demonstrated their similarities to those known from literature on various crystalline materials with impurities. Also, some specifics of the present system were shown in considerable bias dependences of impurity bands and of critical concentrations for their formation. These dependences can be further treated to provide some specific phase diagrams in variables "bias-concentration" as it took place in antiferromagnetic insulators where such diagrams in variables "magnetic field-concentration" were quite informative²³. A practical application of the described electronic band structure is suggested in a form of highly sensitive bias control on the system's conductivity through the impurity subband when brought close to a regime of bias-controlled Mott's metal-insulator transition.

Acknowledgements

Y.G.P. is grateful for the support of this work from Portuguese FCT project PTDC/FIS/120055/2010 and M.C.S. is indebted to the support from FCT project PTDC/QUI-QUI/117439/2010. V.M.L. acknowledges partial supports from the European FP7 program by SIMTECH 246937 Grant, by STCU Grant No 5716-2 "Development of Graphene Technologies" and by the Special Program of Fundamental Researches of NAS of Ukraine.

-
- ¹ K.S. Novoselov, A.K. Geim, S.V. Morozov, D. Jaing, Y. Zhang, S.V. Dubonos, I.V. Grigorieva, and A.A. Firsov, *Science* **306**, 666 (2004).
 - ² P.R. Wallace, *Phys. Rev.* **77**, 622 (1947).
 - ³ G. Semenoff, *Phys. Rev. Lett.* **53**, 2449 (1984).
 - ⁴ K.S. Novoselov, E. McCann, S.V. Morozov, V.I. Fal'ko, M.I. Katsnelson, U. Zeitler, D. Jiang, F. Schedin, and A.K. Geim, *Nature Phys.* **2** 177 (2006).
 - ⁵ Y. Zhang, Y.-W. Tan, H.L. Störmer, and P. Kim, *Nature* **438**, 201 (2005); Y. Zhang, T.-T. Tang, C. Girit, Z. Hao, M. C. Martin, A. Zettl, M. F. Crommie, Y.R. Shen, and F. Wang, *Nature* **459**, 820 (2009).
 - ⁶ E.V. Castro, K.S. Novoselov, S.V. Morozov, N.M.R. Peres, J.M.B. Lopes dos Santos, J. Nilsson, F. Guinea, A.K. Geim, and A.H. Castro Neto, *Phys. Rev. Lett.* **99**, 216802 (2007).
 - ⁷ T. Ando and M. Koshino, *J. Phys. Soc. Japan* **78**, 034709 (2009).
 - ⁸ J.D. Bernal, *Proc. R. Soc. Lond. A* **106**, 106 (1924).
 - ⁹ W. Tao, G. Qing, L. Yan and S. Kuang, *Chinese Phys. B* **21**, 067301 (2012).
 - ¹⁰ J. Liu and W. Zhang, *RSC Adv.* **3**, 21943 (2013).
 - ¹¹ R.M. Ribeiro and N.M.R. Peres, *Phys. Rev. B* **83**, 235312 (2011).
 - ¹² J. Slawinska, I. Zasada, and Z. Klusek, *Phys. Rev. B* **81**, 155433 (2010).
 - ¹³ A. Ramasubramaniam, D. Naveh, and E. Towe, *Phys. Rev. B* **84**, 205325 (2011).
 - ¹⁴ J. Nilsson and A.H. Castro Neto, *Phys. Rev. Lett.* **78**, 126801 (2007).
 - ¹⁵ A. Feher, E. Syrkin, S. Feodosyev, I. Gospodarev, E. Manzhelii, A. Kotlar and K. Kravchenko, in: "Nanotechnology and Nanomaterials. New Progress on Graphene Research", Ed. Jian Ru Gong, InTech (2013), Ch. 5.
 - ¹⁶ S.M. Sze, *Physics of Semiconductor Devices*, NY: Wiley (1969).
 - ¹⁷ B.I. Shklovskii and A.L. Efros, *Electronic Properties of Doped Semiconductors*, Berlin: Springer-Verlag (1984).
 - ¹⁸ M.A. Ivanov and Y.G. Pogorelov, *Sov. Phys. JETP*, **61**, 1033 (1985).
 - ¹⁹ P. Soven, *Phys. Rev.* **156**, 809 (1967).
 - ²⁰ K. Carva, B. Sanyal, J. Fransson, O. Eriksson, *Phys. Rev. B* **81**, 245405 (2010).
 - ²¹ Y. Zhang, A. Mascarenhas, H. P. Xin, and C. W. Tu, *Phys. Rev. B* **61**, 7479 (2000).
 - ²² N.F. Mott, *Adv. Phys.* **16**, 149 (1967).
 - ²³ M.A. Ivanov, V.M. Loktev, Y.G. Pogorelov, *Phys. Reports* **153**, 209 (1987).
 - ²⁴ V.L. Bonch-Bruевич and S.V. Tyablikov, *The Green function method in statistical mechanics*. Amsterdam: North-Holland, 1962.
 - ²⁵ E.N. Economou, *Green's Functions in Quantum Physics*, Springer (2006) p. 87.
 - ²⁶ P.T. Araujo, M. Terrones, M.S. Dresselhaus, *Materials Today* **15**, 98 (2012).
 - ²⁷ I.M. Lifshitz, S.A. Gredeskul, and L.A. Pastur. *Introduc-*

- tion to the Theory of Disordered Systems. Wiley, NY, 1988.
- ²⁸ H. P. Dahal, A. V. Balatsky, and J.-X. Zhu, Phys. Rev. B **77**, 115114 (2008).
- ²⁹ P.W. Anderson, Phys. Rev. **109**, 1492 (1958).
- ³⁰ D.N. Sheng, L. Sheng, Z.Y. Weng, Phys. Rev. B **73**, 233406 (2006).
- ³¹ P. W. Anderson, Phys. Rev. **124**, 41 (1961).
- ³² R. R. Biswas, S. Sachdev, and D. T. Son, Phys. Rev. B **76**, 205122 (2007).
- ³³ V. M. Pereira, V. N. Kotov, and A. H. Castro Neto, Phys. Rev. B **78**, 085101 (2008).
- ³⁴ C. Bena, Phys. Rev. Lett. **100**, 076601 (2008).
- ³⁵ Y.G. Pogorelov, M.C. Santos, V.M. Loktev, Phys. Rev. B **84**, 144510 (2011).
- ³⁶ Y.G. Pogorelov, M.C. Santos, V.M. Loktev, Phys. Rev. B **88**, 224518 (2013).
- ³⁷ A.F. Ioffe and A.R. Regel, Progr. Semicond. **4**, 26 (1960).
- ³⁸ R. J. Elliott, J. A. Krumhansl, and P. L. Leath, Rev. Mod. Phys. **46**, 465 (1974).
- ³⁹ A. V. Zayats, I. I. Smolyaninov, A. A. Maradudin, Phys. Reports **408**, 131 (2005).
- ⁴⁰ V. V. Mkhitarian and E. G. Mishchenko, Phys. Rev. Lett. **110**, 086805 (2013).
- ⁴¹ Z. Ni, Q. Liu, K. Tang, J. Zheng, J. Zhou, R. Qin, Z. Gao, D. Yu, J. Lu, Nano Lett. **12**, 113 (2012).
- ⁴² M. Abramowitz, I. Stegun. Handbook of Mathematical Functions: with Formulas, Graphs, and Mathematical Tables, Washington: National Bureau of Standards (1972), p. 488.

Appendix A

In calculation of the interaction function, Eq. 15, the essential task consists in the integration:

$$\frac{1}{2N} \sum_{\mathbf{k}} e^{i\mathbf{k} \cdot \mathbf{n}} \left(G_{\mathbf{k}}^{(0)} \right)_{jj} = \frac{2 \cos \mathbf{K} \cdot \mathbf{n}}{W^2} \times \int_0^W J_0 \left(\frac{\xi n}{\hbar v_F} \right) \frac{(N_j(\varepsilon) - \xi^2) \xi d\xi}{(\xi^2 - \xi_1^2)(\xi^2 - \xi_2^2)}, \quad (\text{A1})$$

where J_0 is the zeroth order Bessel function, $\xi_{1,2}^2 = \varepsilon^2 + \varepsilon_2^2 \pm \delta^2(\varepsilon)$ are the complex poles of $\det \hat{G}_{\mathbf{k}}^{(0)}$ in ξ -variable and all $|N_j(\varepsilon)| \sim \varepsilon_g^2$ (as seen from Eq. 6). Since this integral is fast converging after $\xi \gtrsim \varepsilon_g$, its upper limit can be safely extended to infinity. Then, after expanding the factor besides the Bessel function in simple fractions:

$$\frac{N_j(\varepsilon, \xi)}{(\xi^2 - \xi_1^2)(\xi^2 - \xi_2^2)} = \frac{N_j(\varepsilon) - \xi_1^2}{\xi^2 - \xi_1^2} - \frac{N_j(\varepsilon) - \xi_2^2}{\xi^2 - \xi_2^2}, \quad (\text{A2})$$

the Hankel-Nicholson integration formula can be applied to each of them:

$$\int_0^\infty \frac{J_0(x) x dx}{x^2 + z^2} = K_0(z), \quad (\text{A3})$$

with the zeroth order MacDonald function K_0 , valid for complex z if $\text{Re} z > 0$ (Ref.⁴²). The z -arguments related to the terms in Eq. A2, can be defined as $z_{1,2}^2 = -\xi_{1,2}^2 (n/\hbar v_F)^2$ and the above requirement will read $\text{Re} \sqrt{-\xi_{1,2}^2} > 0$. For the relevant energy range

$0 < \varepsilon_g - \varepsilon \ll \varepsilon_g$, we can use the choices $\sqrt{-\xi_{1,2}^2} = \sqrt{\sqrt{\gamma^2(\varepsilon) - \varepsilon^2 - \varepsilon_2^2} \mp i \sqrt{\sqrt{\gamma^2(\varepsilon) + \varepsilon^2 + \varepsilon_2^2}}}$. At last, for relevant distances $n \gtrsim r_0$, the resulting $K_0(z_{1,2})$ have big enough arguments, $|z_{1,2}| = |n \xi_{1,2} / \hbar v_F| \gtrsim 1$, to use their asymptotics: $K_0(z_1) \approx -\sqrt{2/\pi z_1} e^{-z_1}$ and $K_0(z_2) \approx \sqrt{2/\pi z_2} e^{-z_2}$. Then, taking account of all prefactors besides these expressions, present in Eqs. 15 and A2, we arrive at the final result of Eq. 15.